









Equatorial Plasma Bubble Occurrence Under Propagation of MSTID and MLT Gravity Waves

H. Takahashi¹ , C. M. Wrasse¹ , C. A. O. B. Figueiredo¹ , D. Barros¹, I. Paulino² , P. Essien¹ , M. A. Abdu¹ , Y. Otsuka³ , and K. Shiokawa³ 

¹Instituto Nacional de Pesquisas Espaciais, São José dos Campos, Brazil, ²Unidade Acadêmica de Física, Universidade de Campina Grande, Campina Grande, Brazil, ³Institute for Space-Earth Environmental Research, Nagoya University, Nagoya, Japan

Key Points:

- We observed equatorial plasma bubbles (EPBs), traveling ionospheric disturbances (MSTIDs), and MLT-gravity waves in the evening period
- A direct evidence of the northeastward propagation of MSTID and EPB seeding process during the solar terminator passage was observed
- We concluded that the observed MSTID was induced by a secondary gravity wave from dissipation of primary waves in the thermosphere

Supporting Information:

- Movie S1

Correspondence to:

H. Takahashi,
hisao.takahashi@inpe.br

Citation:

Takahashi, H., Wrasse, C. M., Figueiredo, C. A. O. B., Barros, D., Paulino, I., Essien, P., et al. (2020). Equatorial plasma bubble occurrence under propagation of MSTID and MLT gravity waves. *Journal of Geophysical Research: Space Physics*, 125, e2019JA027566. <https://doi.org/10.1029/2019JA027566>

Received 23 OCT 2019

Accepted 24 AUG 2020

Accepted article online 30 AUG 2020

Abstract We observed a signature of equatorial plasma bubbles (EPBs) followed by a medium-scale traveling ionospheric disturbance (MSTID) crossing the solar terminator over the geomagnetic equator during the period of post-sunset rise (PSSR) of the F layer. Simultaneous observations of the EPBs and the MSTIDs by ground-based Global Navigation Satellite System receivers and OI 630-nm imagers, ionospheric parameters by ionosondes, and mesosphere–lower thermosphere (MLT) gravity waves (MLT-GWs) by OH airglow imagers have been carried out in the equatorial and low-latitude region of Brazil. On 16–17 September 2015, MSTIDs with very fast horizontal phase speeds, propagating toward northeast (NE), were observed over the latitude region of 0–30°S in the afternoon to evening time zone. It was geomagnetically quiet time (Kp: 2–3). An EPB development was observed after one of the MSTIDs crossed the solar terminator at 22:00 UT. Large-scale MLT-GWs with slower phase speeds were also observed both at São João do Cariri (7.5°S, 35.0°W) propagating from southwest (SW) to NE and Cachoeira Paulista (22.7°S, 45.0°W) propagating northward. This is to report on what we consider as a signature of direct seeding of EPBs by an MSTID that was likely induced by a secondary GW from tropospheric deep cloud convections to the south. This study highlights a possible dynamical process from the troposphere to ionosphere via this vertical coupling process over the 2,500 km of horizontal distance.

1. Introduction

Equatorial plasma bubbles (EPBs) are known to be ionospheric plasma depletions aligned along the geomagnetic field lines extending a few hundreds to thousands of kilometers centered at the geomagnetic equator in the evening to night time zone. It is generated by Rayleigh-Taylor instability (RTI) occurring in the F layer bottom height during the post-sunset rise (PSSR) of the F layer driven by the pre-reversal enhancement (PRE) of the zonal electric field originating from the F layer dynamo (Kelley, 2009). In a typical physical condition of the post-sunset equatorial ionosphere, the EPBs start to develop soon after the local sunset. The fossil remnants of the EPBs that follow the growth phase of the bubble sometimes may last up to dawn. The phenomenon of the post-sunset ionospheric irregularities in the equatorial and low latitude regions was first reported by Booker and Wells (1938). McClure et al. (1977) observed plasma depletions in the ion density measured on board the Atmospheric Explore Satellite (AE-C) and named them “plasma bubbles.” The plasma depletions along the magnetic meridian were observed by Weber et al. (1978). Sahai et al. (1981) reported airglow 630.0-nm depletions from the ground-based observation and concluded that they were due to plasma bubbles. Morphology and physical characteristics have been extensively investigated not only by observations (e.g., Abdu et al., 2009; Sobral et al., 2002) but also by simulation studies (e.g., Huba & Joyce, 2010; Yokoyama, 2017). The current interest for the investigation of the EPBs arises from the fact that the plasma irregularities associated with such large-scale plasma depletions may cause scintillations of the radio waves in telecommunications and in positioning errors for the Global Navigation Satellite System (GNSS) satellite-based navigation systems. For the above reasons, the ionospheric weather information is one of the major issues in space-based technology applications.

Although the general characteristics of the EPB phenomenology have been well studied, some important issues remain unsolved (e.g., the EPB seeding process and development conditions as a function of the local time and longitude). It appears that several factors control the occurrence of plasma bubbles. One of them is the ionospheric conditions for the development of the RTI process. It is now well known that the

development of the RTI mainly depends on upward drift velocity of the F layer, steepness of the F layer bottom side, and the F2 layer peak altitude because of the height-dependent (decreasing with height) ion-neutral collision frequency. Another factor is the dynamical influence in the F layer bottom side due to gravity wave (GW) input acting as a seeding source to kick off instability growth. Regarding the effect of upward drift velocity, Abdu (2005) reported that a vertical velocity of 20 m/s is a threshold level to start the RTI. Huang (2018), in his review work, pointed out that the generation of equatorial spread F (ESF) and plasma bubbles could occur even for an upward drift velocity lower than 20 m/s. Some additional upward forcing such as due to GWs, in addition to the normal PSSR of the layer, would be helpful to generate the RTI condition. Tsunoda et al. (2011, 2018) have proposed the presence of large-scale wave structure (LSWS) along the geomagnetic equatorial zone as a requirement for initiating the RTI process. Tulasi Ram et al. (2014) investigated the characteristics of the LSWS using temporal variations of total electron content (TEC) observed from the ground-based Communications/Navigation Outage Forecasting System (C/NOFS) satellite data. They found a zonally oscillating structure of the TEC, of which the amplitude increased toward the sunset terminator. When a wave crest meets the solar terminator under the condition of the PSSR, the upward drift velocity will be enhanced, resulting in stronger instability growth. The PSSR driven by the PRE could vary with season, depending on the angle between solar terminator and geomagnetic meridian (Abdu et al., 1981) and solar flux. On the other hand, the modulation of the PSSR by local dynamical process, such as GWs and LSWS, could produce day-to-day variability in the EPB occurrence.

One of the origins of medium-scale traveling ionospheric disturbances (MSTIDs) is known to be GWs in the upper atmosphere (Hocke & Schlegel, 1996; Nicolls et al., 2014; Otsuka, 2018). The amplitude of oscillation in the TEC due to MSTIDs can be in the order of 0.1 to 1 TEC unit (1 TECu = 1×10^{16} electrons/m² column) (Figueiredo et al., 2018). Takahashi et al. (2018) studied possible relationship between propagation of the MSTIDs and generation of the EPBs. They compared the horizontal wavelength of the observed MSTIDs and the inter-EPB distances and found a certain level of positive correlation and suggested that the MSTIDs could be one of the dynamical processes to modulate the EPB generation and the interbubble distances. However, a direct signature of EPB seeding by MSTIDs has not been reported yet. In the present work, therefore, we further investigate the contribution of MSTID in the EPB seeding process. We looked for a case when an EPB was generated in association with an MSTID crossing the solar terminator.

In order to achieve the above-mentioned purpose, simultaneous observations of the three dynamical phenomena, EPBs, MSTIDs, and mesosphere–lower thermosphere GWs (MLT-GWs), have been carried out using airglow imagers, ionosondes, and ground-based GNSS receivers. The occurrence of the three phenomena (MLT-GW, MSTID, and EPB) on the same day (afternoon to evening time zone) is rare. Takahashi et al. (2018) reported a case of the MSTID and EPB occurrences on the same day in the South American region during the equinox seasons. The observation was made on September 2015 when the MLT-GWs were also present. We found one case of the simultaneous occurrence of the three phenomena. It was in a geomagnetically quiet day. The physical parameters observed in the event will be presented and discussed below.

2. Observations

To monitor seeding and development of EPBs, multiple instrumental observations along the geomagnetic equatorial zone during the afternoon to evening period are necessary. In the present work, OI 630 nm and OH-near-infrared (NIR) airglow all-sky imager data, ground-based GNSS receiver network data, and ionosonde data are used.

2.1. 630-nm and OH-NIR All-Sky Images

Airglow all-sky imagers equipped with an OI 630.0-nm interference filter and an OH-NIR color filter (715–930 nm) notched at 865 nm have been routinely operated, one at São João do Cariri (hereafter Cariri) (7.4°S, 36.5°W) and another at Cachoeira Paulista (hereafter CP) (22.7°S, 45.0°W). The all-sky 630-nm image covers an area of approximately 1,500 km of diameter (75° zenith angle) at an altitude of 250 km. On the other hand, the OH-NIR image covers an area of diameter of 600 km (75° zenith angle) at an altitude of 90 km. The 630-nm image is taken using a time integration of 90 s, whereas the OH-NIR image is taken with

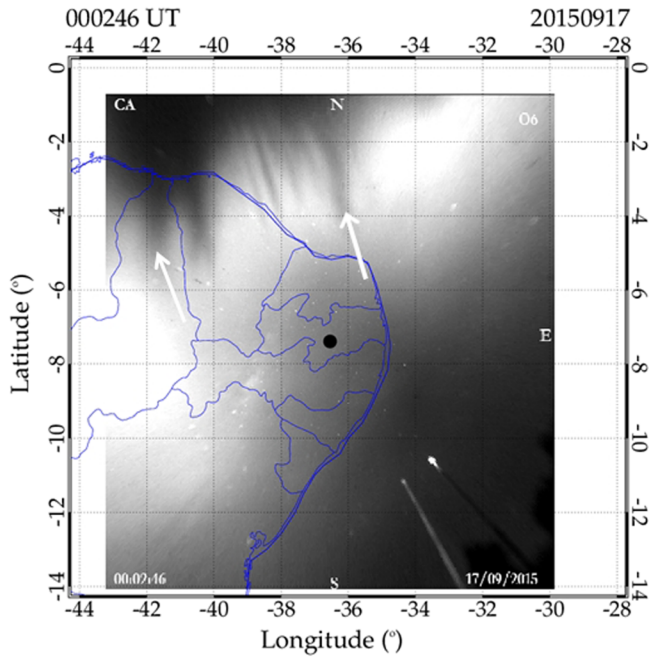


Figure 1. Equatorial plasma bubble signatures observed by airglow 630 imager at Cariri Airglow Observatory (7.5°S, 36.5°W) on 17 September 2015 at 00:02 UT. White arrows indicate development of the bubbles.

15 s. Therefore, the time sequence of the 630-nm and OH-NIR observation is every 2 min, which is enough to resolve the temporal and spatial variations of the plasma bubbles and the MLT-GWs.

The recorded all-sky images are transformed in geographic coordinates as a usual practice. From the sequence of images, a keogram was produced by plotting north–south (east–west) sliced images at a fixed longitude (latitude) as a function of time. Fast Fourier transform (FFT) was applied to calculate the wave characteristics, the horizontal wavelength, the phase velocity, the period, and propagation direction. Data processing and analysis have been presented elsewhere (Takahashi et al., 2015).

2.2. The TEC and the dTEC

The ionospheric TEC can be obtained by using a combination of GNSS and ground-based receivers. Phase delay of the received GNSS radio wave is proportional to the TEC integrated along the propagation path, as given by $dS = 40.3[TEC]/f^2$ where dS is a phase delay in meter, $[TEC]$ is in the TEC unit, and “ f ” is a carrier frequency (cycle/s) of the GNSS radio wave. Details of the process of TEC calculation have been reported elsewhere (Takahashi et al., 2016). The magnitude of the TEC depletions during the passage of the EPBs is large, being of the order of 10% of the ambient TEC value. The TEC depletions are magnetic field aligned and thus extend along the magnetic meridian. Therefore, it is relatively easy to recognize/identify

the presence of EPBs from the geographical mappings of the TEC. On the other hand, the normal amplitude of the TEC variation during a passage of the MSTIDs is much smaller, varying from 0.1 to 1 TECu

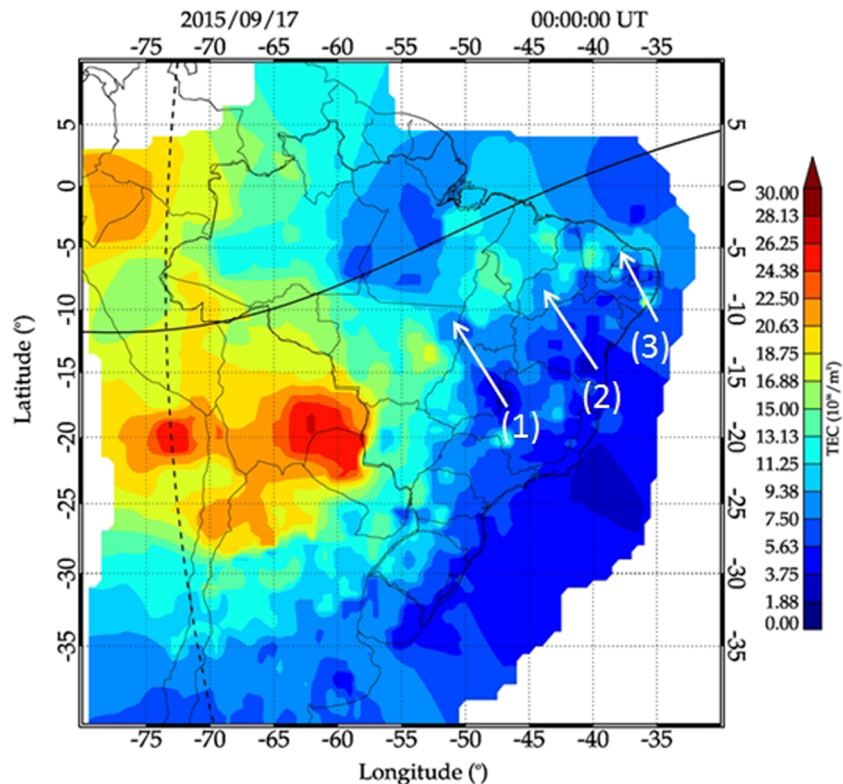


Figure 2. Equatorial plasma bubble signatures (white arrows) observed by TECMap on 17 September 2015, at 00:00 UT. The black line is the geomagnetic equator and the dotted line is solar terminator at 300-km altitude.

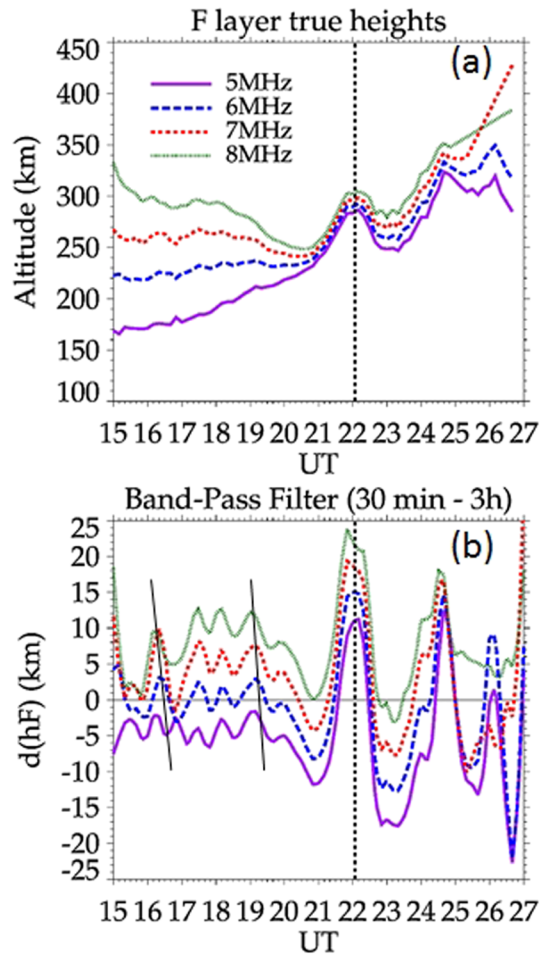


Figure 3. (a) Temporal variations of ionosonde fixed frequency true heights of 5, 6, 7, and 8 MHz observed at São Luís (2.6°S, 44.2°W, geomag. lat. 3.9°S) on 16–17 September 2015; (b) band-pass filtered variations of the fixed frequency true heights. The two black lines show peaks of the 5, 6, 7, and 8 MHz oscillations. The vertical dotted lines are solar terminator crossing at 45°W.

elongated needle-like depletions, over the geomagnetic equatorial region (top left of the image), is a signature of spatially periodic depletions of the F layer plasma density. Horizontal spacing between them is on the average 82 ± 10 km. The depletions, which might be due to oscillation of the F layer bottom height, did not develop in the latitudinal direction before 22:30 UT. After 22:50 UT (19:50 LT), two of them, one at around 36°W and the other at around 42°W, indicated by the white arrows, started to develop toward the zenith of the observatory leading to a form of EPB. The longitudinal distance between the two depletions is estimated to be 805 ± 50 km (assuming that the OI 630-nm emission altitude was at 250 km as mentioned in the previous section). The large error range is due to the uncertainty in the definition of peak of the bubbles.

Figure 2 shows a TECMap taken on the night of 16–17 September 2015 at 24:00 UT (00:00 UT on 17 September). Three depletion structures in plasma density displaced along the magnetic equator (indicated by the white arrows) may be noted. One of them is a newly formed EPB that can be seen at around 55°W intersection with the magnetic equator, denoted as (1) in the figure. The second one, denoted (2), is located at around 47°W and the third one (3) at around 40°W over the magnetic equator. There is a depletion around (7.5°S, 40°W), which seems to be forming another EPB, but it disappeared after ~20 min. The interbubble distance for Bubbles (1) and (2) is estimated as 807 ± 40 km. Bubbles (2) and (3) also have a similar separation (700 ± 40 km). Due to the low spatial resolution of the TECMap in the equatorial region (0–10°S), an interbubble distance shorter than 100 km could not be resolved in the map.

(Figueiredo et al., 2018). In order to visualize such low amplitude of the TEC variations, we calculated the de-trended TEC (dTEC) as

$$(dTEC)_t = (TEC)_t - \langle TEC(t \pm 30 \text{ min}) \rangle$$

where $\langle \rangle$ indicates a running average of 1-min TEC values for ± 30 min. The time series of the TEC data from each satellite and receiver combination have a duration of 3–4 hr. Therefore, temporal oscillation with less than 1-hr period can be retrieved from the data. The dTEC map is prepared by plotting the $(dTEC)_t$ at a pierce point in the ionospheric height at 350 km.

2.3. The Ionosonde Data

Two ionosondes (DIGISONDE:DPS-4) are being operated near the magnetic equator in Brazil, one at São Luís (2.6°S, 44.2°W, geomag. lat. 3.9°S) and the other at Fortaleza (3.9°S, 38.4°W, geomag. lat. 6°S). The digital sounder has 500-W peak power, covering a frequency range from 0.5 to 30 MHz. Ionograms are taken at a cadence of 10 min. The São Luís ionosonde is located 5.8° (~640 km) west of the Fortaleza ionosonde. Therefore, waves in the ionosphere propagating in the longitudinal direction can be monitored by the two ionosondes.

3. Results

In order to study the simultaneous occurrences of the EPB and MSTID in the ionosphere and the GWs in the MLT region, we selected a specific day when all of them could be observed. In a previous work, Takahashi et al. (2018) reported that the occurrence of EPBs and MSTID on the same day was observed mainly in the equinox seasons, around March and September. In the present work, we therefore selected a day of observation, that is, 16 September 2015.

3.1. Equatorial Plasma Bubbles

Figure 1 shows an all-sky image of the OI 630-nm atomic oxygen emission observed at Cariri on the night of 16–17 September 2015 at 00:02 UT (21:02 LT at 45°W). The dark band structure with several

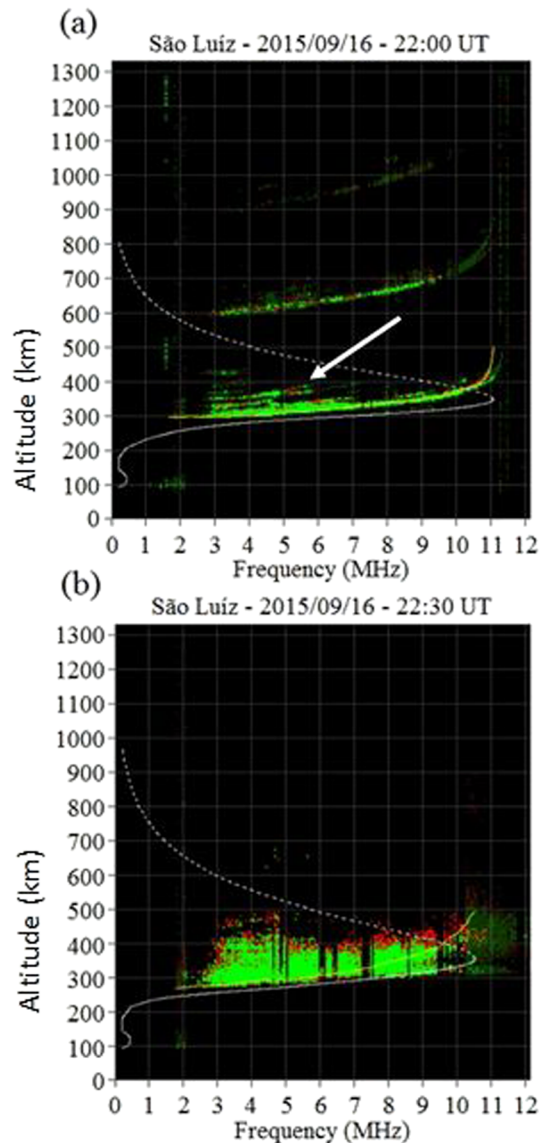


Figure 4. Ionogram at São Luís on the night of 16 September 2015 at (a) 22:00 UT and (b) 22:30 UT. The white arrow indicates the satellite traces.

The interbubble distance of 807 km, observed here, is somewhat longer than those previously reported. Takahashi et al. (2009) measured it in a range of 100 to 300 km and Makela et al. (2010) reported such distance to be between 100 and 700 km. Both the observations have used the OI 630-nm all-sky imager. The field of view of the imager (~1,500 km) limits the measurement of interbubble distances shorter than 700 km. On the other hand, Barros et al. (2018) measured the distance to be between 640 and 920 km using TECMap. Our present case is in the range of the previous observations.

3.2. Medium-Scale Traveling Ionospheric Disturbances

The ionospheric condition on this evening can be noted in the ionosonde data from São Luís as shown in Figure 3. A large peak at 22:00 UT in the ionospheric oscillation (Figure 3a) is present during the evening uplift of the F layer due to the PRE of the zonal electric field. The fixed frequency true heights (at 5–8 MHz), obtained from the ionograms as read by the SAO explorer, showed periodic oscillations with a period of ~45 min between 16:00 to 20:00 UT (Figure 3b). It may be noticed that there is a phase lag between the isolines at different frequencies from top to down (clearly noticeable during the daytime hours). Two straight lines passing through the crest of the 8-MHz isoline to that of the 6 MHz in Figure 3b indicate a time lag with decrease in the frequency, which might suggest that an atmospheric GW was propagating upwards in the height region of 200 to 300 km during the period. From the ionograms, we also obtained the virtual height of F layer bottom side ($h'F$) at 22:00 UT as 290 km, and the maximum vertical drift velocity was 18 m/s at around 21:40 UT. Although the uplifting was clear to see, the associated vertical drift velocity (18 m/s) and the virtual height of F layer bottom side (290 km) were somewhat low, not providing a favorable condition for the generation of EPBs as expected from previous studies (Abdu et al., 2009; Huang & Hairston, 2015). Nevertheless, the ionogram over São Luís registered a satellite trace structure at 22:00 UT, pointed by a white arrow in Figure 4a, indicating that the F layer bottom height has a wave structure at this moment. Half an hour later at 22:30 UT, spread F occurred (Figure 4b). Ionograms at Fortaleza (not shown here) also showed a similar oscillation with a time lag by approximately 15 min relative to São Luís. It indicates that there was a GW propagation eastward in the bottom side of the F layer during the period of 18:00 to 22:00 UT.

In order to see the signature of the ionospheric wave-like perturbation, we calculated the $dTEC$ variations from the ground-based GNSS receiver data, as mentioned in the previous section. The $(dTEC)_t$ values are color coded and plotted as a map in the geographic coordinates. Figure 5 shows the $dTEC$ map of a square area bounded by 0–15°S and 30–50°W at 21:48 UT. The color shade indicates the TEC variation from -0.4 (blue) to +0.2 (red) TECu. Owing to a small number of ground-based GNSS receiver in this region, the spatial resolution of 140 km and a time integration of 2 min are used. In the map, one can see a wave front (red squares) with the oscillation amplitude of 0.2 TECu elongated from (9°S, 48°W) to (13°S, 40°W), circled by ellipses. The arrow indicates the direction of wave propagation. The black dotted line at around 41°W indicates the solar terminator at 300-km altitude at that time. It is interesting to note that the wave front and the solar terminator crossed at around 45°W at 22:00 UT when the F layer peak ($hmF2$) was at 340 km.

To better visualize movement of the phase fronts, keograms using the time series of $dTEC$ maps are plotted. Figure 6 presents a longitudinal cut of (30–50°W) at a fixed latitude of 5°S (upper panel) and a latitudinal cut (0–30°S) at a fixed longitude of 40°W (lower panel) as a function of time from 17:00 to 24:00 UT on 16

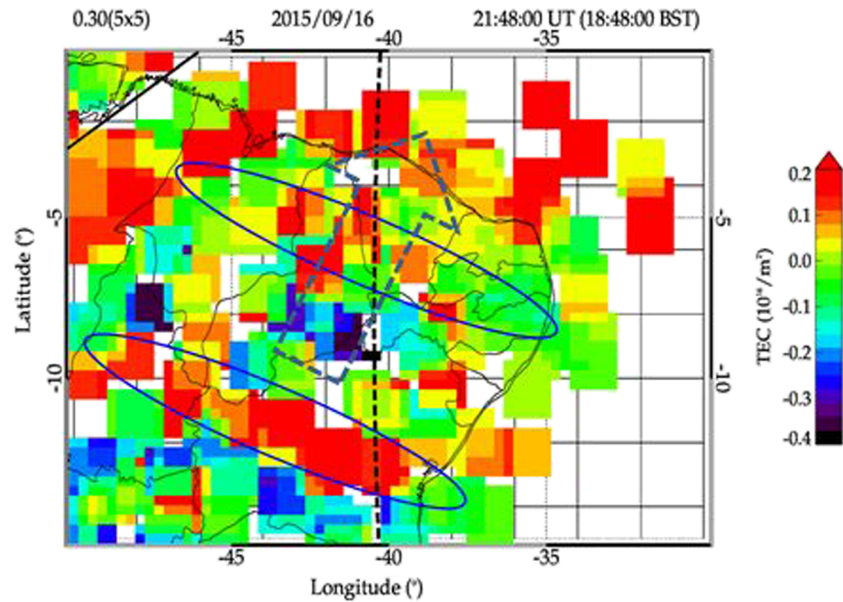


Figure 5. Color shade map of dTEC over the area 0–15°S by 30–50°W on 16 September 2015 at 21:48 UT. The dotted line indicates the solar terminator at 300-km altitude. The elliptical circles indicate location of wave crests. The arrow indicates the direction of wave propagation.

September 2015. We may note several propagation forms in the 20:00 to 22:30 UT time zone (highlighted by a blue line box). The thin black lines (four lines in the upper and lower panels) indicate movement of the

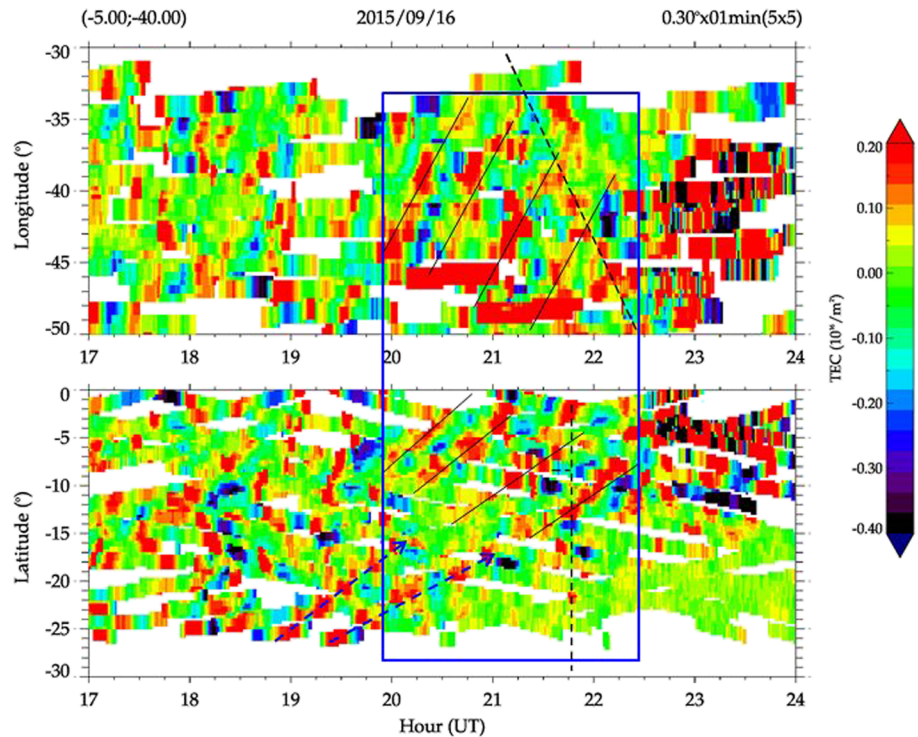


Figure 6. Keogram of dTEC map in the 30–50°W (upper panel) and 0–30°S regions (lower panel) on 16 September 2015 from 17:00 to 24:00 UT. The square box highlighted by blue line is to calculate wave characteristics of MSTID. The black lines indicate the movement of the wave crests of the zonal components (upper) and the meridional components (lower). The blue dashed arrows indicate movement of the phase fronts from 25°S. The black dashed lines indicate the solar terminator line.

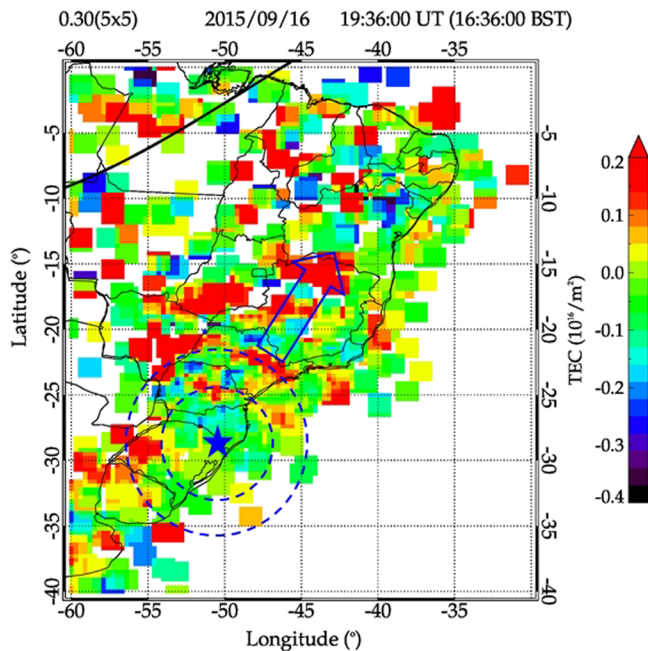


Figure 7. Color shade map of dTEC over the area of (0–40°S) by (30–60°W) on 16 September 2015 at 19:36 UT. Two circles are plotted on the curved wave crests. The center of the circles is located at around (29°S, 51°W). The blue arrow indicates the direction of wave propagation.

wave fronts, which are aligned in the NW–SE direction, toward the NE direction. The disturbed dTEC features after 22:30 UT may indicate the beginning of the EPB activity. The dashed black lines indicate the solar terminator at 300-km altitude. A wave structure seen in the 21:30–22:30 UT time interval is what we observed in Figure 5. In order to get the wave characteristics, we used the FFT spectral analysis (Figueiredo et al., 2018) for the 20:00 to 21:30 UT time zone. The results showed the following properties of the waves: the horizontal wavelength (λ_h) of 689.4 ± 47.1 km, the wave period of 35.7 ± 1.8 min, the phase velocity of 322.1 ± 27.3 m/s, and the azimuth of the propagation direction of $31.3 \pm 8.4^\circ$.

It is interesting to note that in the lower panel of Figure 6, there are two crests, indicated by blue dashed line arrows, starting at around 25°S, one from 19:00 and the other from 19:30 UT, and each of them moving toward north. It indicates that there are two waves starting from the south of 25°S and propagating northwards. Although there are some discontinuities in the crests at around 20:15–20:30 UT (it might be due to interference of the other waves coming from the low latitudes), these two waves appear to propagate to the 0–15°S region after 21:00 UT. In Figure 7, the dTEC map of the 0–40°S region at 19:36 UT is presented. It is clear to see two curved wave fronts extended at around 20–25°S propagating toward NE. For reference, two circles (broken blue lines) are plotted along the phase fronts. It is worth noting that the center of the concentric circles is located at around (29°S, 51°W), suggesting a source region of the concentric

waves. For better viewing the wave propagation, a short video of dTEC map between the 19:00 and 20:00 UT period was presented in Movie S1. Using keograms with a cut at 22.5°S and 50°W (not shown here), the wave characteristics of the concentric waves were calculated as the horizontal wavelength (λ_h) of 646.3 ± 52.2 km, the wave period of 23.7 ± 1.2 min, the phase velocity of 455.1 ± 43.2 m/s, and the azimuth of the propagation direction of $25.8 \pm 10.4^\circ$. These are almost the same as that observed at 0–15°S (Figure 5), suggesting that the MSTIDs observed in the equatorial region (5°S) could be concentric waves originating from 30°S.

Such concentric waves in the ionosphere have been reported earlier by Nishioka et al. (2013) and Azeem et al. (2015). They attributed them to the MSTID generated by atmospheric GWs originating from tropospheric cloud convections. As to be mentioned later, in the present case, there was a tropospheric convection system located around 30°S. It should be noted that the concentric wave forms are clear to see in the northern part of the fronts, but not in the southern part. This might be due to an effect of background wind as discussed by Nishioka et al. (2013). Fully concentric waves can be observed only under the condition of low background winds whereby Doppler effects do not occur significantly (Vadas et al., 2009).

3.3. Mesosphere–Lower Thermosphere Gravity Waves

From the evening to nighttime on 16 September, there were mesospheric GW activities observed by an OH-NIR imager at Cariri. Figure 8a presents a snapshot of the OH image at 23:37 UT. Short band-structured waves ($\lambda_h \sim 30$ km) can be seen. From the sequence of images, keograms of the E–W and N–S cuts of the OH images were made, which are shown in Figure 8b. Longitudinal and latitudinal coverage of the keograms are referred to ~ 120 km. In addition to the monochromatic short waves (period of 6–9 min), a longer period (>1 hr) wave structure can be noticed. Wave characteristics were calculated using the N–S and E–W keograms, applying the FFT analysis, which is shown in Figure 8c. The process of calculation has been reported elsewhere (Figueiredo et al., 2018, Appendix A). The wave characteristics are the following: the horizontal wavelength of 569 ± 32 km, the wave period of 89 ± 5 min, the phase speed of 106 ± 8 m/s, and the azimuth of the wave propagation of $34 \pm 1^\circ$.

On the same evening, a similar wave structure in the OH image was also observed over CP, which is located at $\sim 1,900$ km southwest of Cariri. The OH image at 23:25 UT, the N–S and E–W keograms, and the FFT

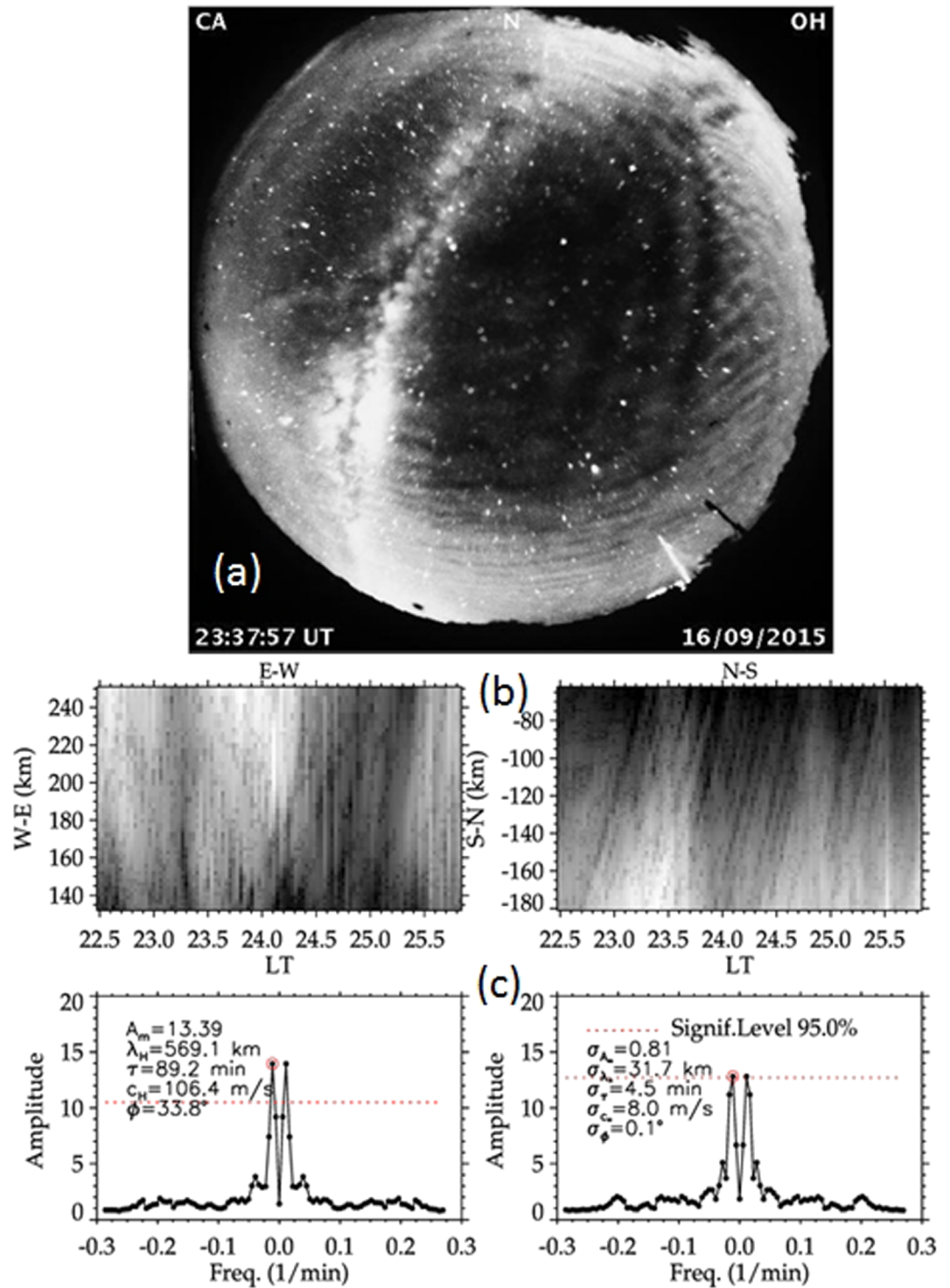


Figure 8. (a) All-sky image of airglow OH NIR observed at Cariri (7.4°S, 35.6°W) on the night of 16 September 2015 at 23:37 UT. (b) Keograms of the E-W and N-S cuts of the images, the distance from the zenith (km) as a function of time (UT), (c) fast Fourier transform spectrum of the keograms, and wave characteristics.

spectra are shown in Figure 9. The wave characteristics are the following: the horizontal wavelength of 583 ± 30 km, the wave period of 55 ± 3 min, and the phase speed of 178 ± 15 m/s, with the propagation direction almost to north ($0.5 \pm 12^\circ$). If we compare the wave characteristics between CP and Cariri, there

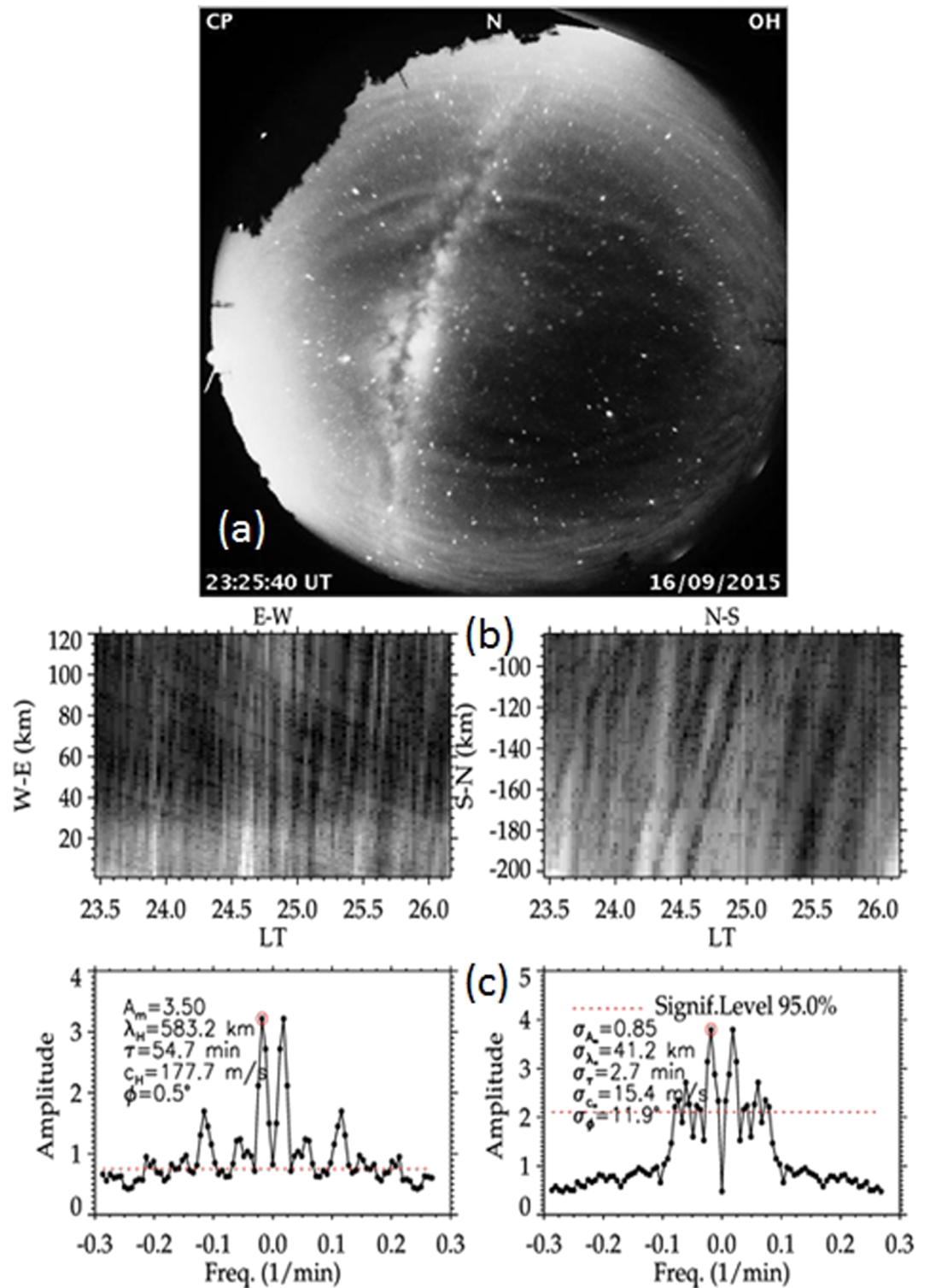


Figure 9. Same as Figure 8, except for Cachoeira Paulista (CP) (22.7°S, 45.0°W).

is a similarity on the long horizontal wavelength (570–580 km), but the period is longer and the phase speed is lower at Cariri. The propagation directions are toward north at CP and northeast at Cariri. These similarities and the difference of the observed GW characteristics between the two distant sites suggest

Table 1

Characteristics of Observed EPBs and MSTIDs in the Ionosphere and Mesosphere–Lower Thermosphere (MLT) Gravity Waves, Observed at São Luís (2.6°S, 44.2°W), Cariri (7.6°S, 36.5°W), and Cachoeira Paulista (CP) (22.7°S, 45.0°W)

Parameters	Wavelength or interval (km)	Period (min)	Phase velocity (m/s)	Propagation direction (° from N)	Observed time interval (hs–hs) UT ^a
Interbubble distance/TECMap in the range of (0–15°S, 35–50°W)	807 ± 40				23:00–24:00
Interbubble distance/630 imager at Cariri in the range of (0–6°S, 36–44°W)	805 ± 50				23:00–24:50
MSTID/dTEC at 0–15°S	689 ± 47	35 ± 2	322 ± 27	31 ± 8	20:00–21:30
MSTID/dTEC at 20–30°S	646 ± 50	24 ± 3	455 ± 20	26 ± 10	19:00–20:00
hF true height oscillation/ionogram at São Luís		45 ± 10			18:00–20:00
MLT gravity waves/OH imager at Cariri	(1) 31.5	8.9	58.7	313	22:40–23:20
	(2) 33.0	12.1	45.5	105	23:23–00:16
MLT gravity waves/OH imager at CP	(3) 569 ± 32	89 ± 5	106 ± 8	34 ± 1	22:30–01:40
	(1) 26.6	7.1	62.8	9.0	23:16–00:21
	(2) 583 ± 30	55 ± 3	178 ± 15	0.5 ± 12	23:30–02:10

Note. The bold values are those discussed in the present work.

^aObserved time interval used for the spectral analysis.

that the GWs observed at CP and Cariri are different, but they might be from the same origin from the south of CP, since the period will increase with horizontal distance at a given altitude for GWs from a deep convective plume (Vadas et al., 2009).

4. Discussion

During the afternoon to evening hours of 16 September 2015, which was a geomagnetically quiet day (Kp: 2 to 3+), we observed the propagation of an MSTID, in the form of a periodic perturbation of F layer bottom side heights that was followed by development of EPBs. Also observed concurrently were MLT-GWs, whose propagation direction was similar to that observed for the MSTID. Based on the auroral activity indices, no energy input from the high-latitude region was expected. In Table 1, the characteristics of the observed EPBs, MSTIDs, and MLT-GWs are summarized for comparison. Some similarities between the interbubble distances and horizontal wavelengths of the MSTIDs and between the MSTIDs and MLT-GWs called our attention to further investigate the relationship between them.

4.1. Relation Between the MSTIDs and the EPBs

It is interesting to note that the observed interbubble distance of 805 ± 50 km, as obtained from both the TECMap and airglow 630-nm imager, might be related to the horizontal wavelength of the MSTID, which is 689 ± 47 km. If one considers the wave propagation direction (azimuth) of 31° and takes a component perpendicular to the geomagnetic meridian (-18° at 45° W), the distance between the crests can be estimated to be 912 ± 150 km. This is within the error range of the observed interbubble distances. On the other hand, if we consider the westward movement of the solar terminator against the eastward movement of the crest of MSTID, the interbubble distance could be shorter as pointed out by Huang et al. (2013). Nevertheless, the present result might suggest a contribution of the MSTID in seeding the EPB.

Another point to be noted is that, as shown in Figures 5 and 6, one of the crests of the MSTID crossed the solar terminator at 45° W longitude during the uplifting of the F layer at 22:00 UT. The encounter of the two events could accelerate the upward drift velocity of the layer, which could provide a favorable condition for a seed perturbation to grow into EPB by the RTI mechanism. Tsunoda et al. (2011) observed zonally extended LSWSs in the western Pacific equatorial region during the evening period. The observed zonal wavelengths were around 300 to 800 km. Tsunoda (2015) concluded that these are zonally extended periodic upwelling of the F layer bottom height, generated most probably by atmospheric GWs propagating upward from the lower atmosphere. According to Tsunoda (2015), the LSWS is confined to the early evening period, prior to the sunset rise (PSSR) of the F layer, and it is stationary, or has very low phase velocity. Our presently observed MSTID is different from the LSWS observed by Tsunoda et al. (2011). Nevertheless, the effect to accelerate or decelerate F layer uplifting during the PSSR period might be same. As far as we understand,

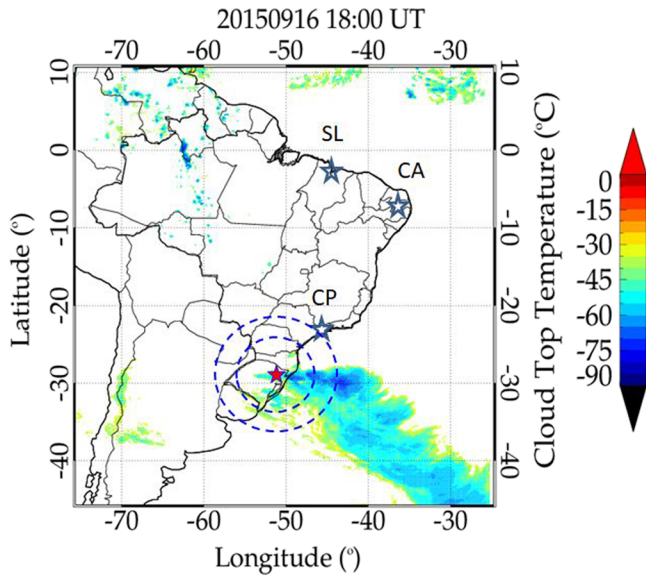


Figure 10. Cloud top temperature map over South America at 18:00 UT, 16 September 2015, produced by Center for Weather Forecasting and Climate Studies (CPTEC/INPE) based on NOAA GOES 13 satellite data. Deep cloud convection system can be seen over the south of Brazil (~29°S). The red star and dashed circles are location of the concentric MSTID presented in Figure 7. The blue star marks are location of the ground-based observatories at Cachoeira Paulista (CP), Cariri (CA), and São Luís (SL).

this is the first reporting on the visualization of the propagation of MSTID crossing the sunset terminator leading to the seeding of EPBs.

4.2. Source and Propagation of MSTIDs

We observed a large-scale MSTID in the low latitudes (5–10°S) (Figure 5), which might contribute to seed the EPBs. From the similarity of the characteristics and the propagation direction between the observed MSTIDs at 20–25°S and 5–10°S as shown in Table 1 and Figure 6, we conclude that the observed MSTIDs are the same as that which started around (29°S, 51°W) as shown in Figure 7. It is well known that the ionospheric MSTIDs are induced by atmospheric GWs in the thermosphere (Hocke & Schlegel, 1996). To find out possible GW sources, we looked for some meteorological activity in the troposphere. Figure 10 presents a map of the cloud top temperature over South America at 18:00 UT, on 16 September 2015, produced by the Center for Weather Forecasting and Climate Studies (CPTEC/INPE) based on NOAA GOES 13 satellite data (<http://satellite.cptec.inpe.br/home/index.jsp>). The dark blue region located at around 28–32°S shows the temperature to be lower than –60°C, indicating a deep cloud convection system. For reference, the center of concentric waves and two circular wave fronts (of Figure 7) are also plotted in Figure 10. It is clear to see that the center is located at the western corner of the convection area. This strongly indicates that the convection system might be related to generation of the MSTID. It is well known that such cloud convection is one of the most effective sources of generation of the internal GWs in the lower atmosphere (Tsuda et al., 2000; Vadas, Yue, et al., 2009).

The observed MSTID phase velocities, which are 322–455 m/s, are extremely fast. If one assumes that the observed MSTIDs were created by the local GW in the thermosphere as suggested by Fritts et al. (2008) and Otsuka et al. (2013), our question is that from where does it come? According to Vadas et al. (2019), the condition of propagation of a GW from the mesosphere to thermosphere is that the intrinsic phase speed (c_i) should be less than the local sound speed (c_s) with the following relation:

$$c_i/c_s \leq (0.9-0.98)$$

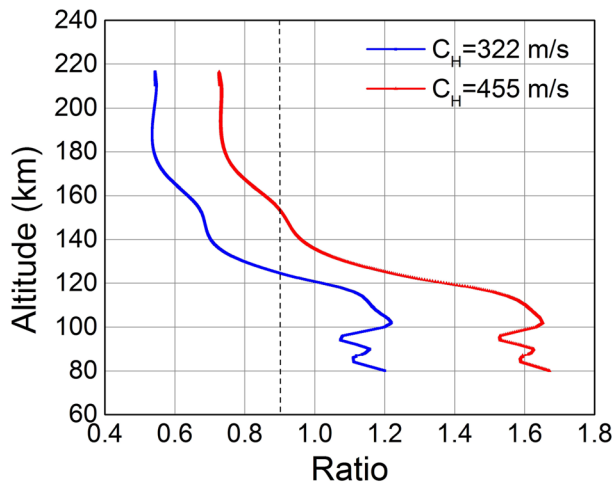


Figure 11. Ratio of the GW intrinsic phase speed (c_i) to the speed of sound (c_s) as a function of altitude for the observed GW phase speeds $c_H = 322$ m/s (blue line) and $c_H = 455$ m/s (red line). A model atmosphere with winds (TIE-GCM) was used. A vertical dashed line indicates the ratio of 0.9.

We calculated the ratio (c_i/c_s) as a function of altitude using the observed GW (MSTID) phase velocities (c_H) of 322 and 455 m/s and the model atmosphere with winds: the Thermosphere–Ionosphere–Electrodynamics General Circulation Model (TIE-GCM) (Roble & Ridley, 1994). The results are presented in Figure 11. The dashed line in the figure shows the ratio of 0.9 which indicates the limit of altitude of the GW propagation. The figure shows that the GWs of $c_H = 322$ and 455 m/s would not have a condition to propagate below the 124- and 153-km altitude, respectively. It means that the present GWs have not been created below 120 km. It is likely to be a secondary GW generated in the thermosphere.

Vadas and Crowley (2010) studied thermospheric GWs related to tropospheric cloud convections. Through the simulation of GW ray tracing, they discovered that most of the observed thermospheric GWs are not primary waves from the troposphere, but secondary GWs generated through thermospheric body forces. Makela et al. (2010) reported that the interbubble distances observed by OI 630-nm imager were between 100 and 700 km and found that the occurrence of

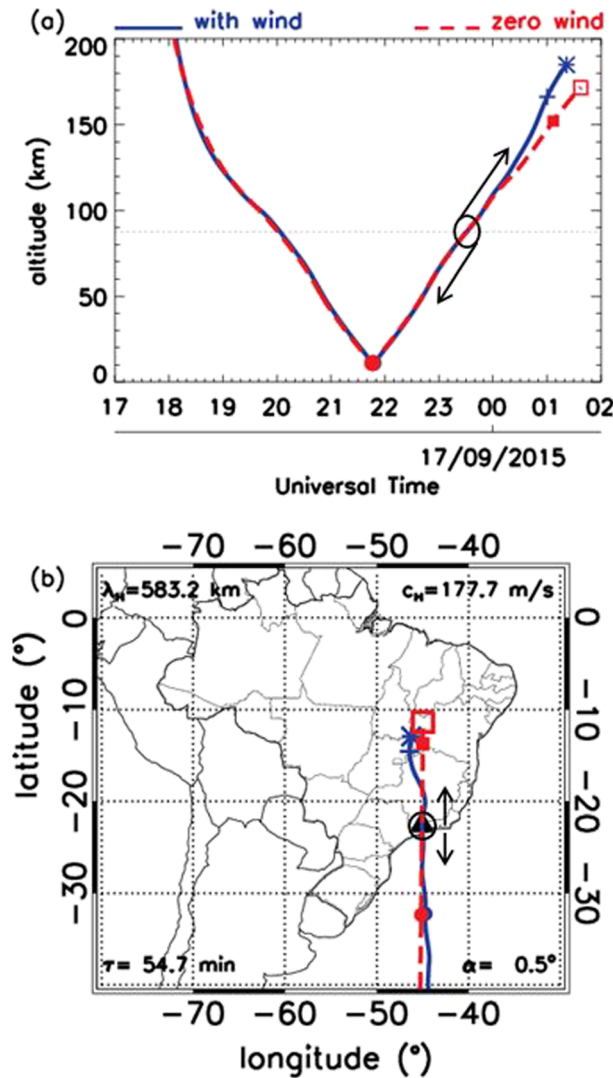


Figure 12. Ray tracing (backward and forward) of the observed gravity wave (λ_h ; 583.2 km) from 87-km altitude at Cachoeira Paulista (22.7°S, 45.0°W) on the night of 16–17 September 2015, for the trajectory of (a) altitude versus time (UT) and (b) latitude versus longitude. Red lines are the result without wind model, and blue lines are the result with background wind model. Black circles are the starting point of the ray tracing, the red squares and blue “+” marks indicate where the wave starts to dissipate, and red “□” and blue “*” represent the positions where the momentum flux reduced to 25% of the maximum value. The red and blue circles indicate the reflection point in the troposphere at around 10-km altitude.

vection activity was observed, then bounced toward southwest, indicating that the source of the GWs was further south.

The forward ray tracing for the observed GWs is shown in Figure 12a. It indicates that the wave might propagate upward until an altitude at around 150 km without decreasing the momentum flux and then starts to dissipate losing the wave amplitude (25% of the maximum value) at around 170–180 km. It also indicates that the wave took around 3 hr to reach an altitude of 160 km. One may note that the F layer bottom height in this evening (19:00–20:00 UT) was above 200-km altitude (Figure 3a). Therefore, it is not plausible to assume that the observed GWs in the MLT region were responsible for perturbation of the F layer bottom height inducing the MSTID. Further to it, there is a large difference in the phase speed between the

interbubble distances coincided to the secondary generated GW spectra simulated by Vadas and Crowley (2010). Our present results agree well with what they concluded. On the other hand, Azeem et al. (2015) observed concentric GWs in the stratosphere, mesosphere, and ionosphere, simultaneously, over North America. The observed MSTID was the horizontal wavelength of 251 km, period of 20.8 min, and the phase velocity of 201 m/s. The horizontal wavelengths of the GWs in the mesosphere and stratosphere were also similar (200–300 km). They suggested that these GWs were likely generated by a same convection system. In contrast to Azeem et al. (2015), our present MSTID might have been induced by a secondary GW created by the dissipation of primary GWs from the deep convection system.

4.3. Mesosphere–Lower Thermosphere Gravity Waves

We observed long horizontal wavelength MLT-GWs both at 7.4°S (Cariri) and 22.7°S (CP). Considering the similarity of wave characteristics and propagation directions, it seems that both the sites observed a same GW. It means that the wave propagated more than 2,000 km. Therefore, we looked for a source region of this wave activity. In order to trace the MLT-GW trajectory, a wave ray tracing model (Paulino et al., 2012) was applied to the GW with horizontal wavelength of 583.2 km observed over CP. The results of forward and backward ray tracing from the OH emission altitude (87 km) are shown in Figure 12. The model calculates vertical wave number (m^2) and wave amplitude for each step of the height range (backward and forward) checking its propagation condition. The backward ray tracing indicates an altitude of wave reflection or absorption and the forward ray tracing indicates the upper limit of wave propagation. The upper panel (a) shows vertical trajectories with and without wind model. The wind model used in this work was according to the TIE-GCM for above 100 km and Horizontal Wind Model (HWM07) (Drob et al., 2008) from the ground to 100-km altitude. One can notice that the backward ray tracing from 87 km traced down to ~10-km altitude in the troposphere at around 21:40 UT and got reflected.

The horizontal distance of the trajectory is shown in the lower panel (b) (red dot), which is located at around (32°S, 45°W). This falls on the cloud convection zone presented in Figure 10. It is, however, ~600 km east away from the center of MSTID concentric waves. This difference might explain that the two waves have their origin in the convective system but starting at different time and different places. We also applied the ray tracing for the GWs observed at Cariri. The backward tracing, in this case, did show a reflection point on the ground at around 1,400 km southwest of Cariri where no con-

MLT-GW (60–100 m/s) and the MSTID (300–400 m/s), indicating that the former should not be a source of the latter. The observed MLT-GWs might dissipate at around 160–180 km, producing a thermospheric body force that generated secondary waves as suggested by Vadas and Fritts (2002), Vadas and Liu (2009, 2013), and Vadas and Crowley (2010).

As mentioned above, there was a time difference between the observation of MSTID (at around 19:00–22:00 UT) and MLT-GWs (22:30–23:30 UT). Therefore, the observed MLT-GW could not be a primary GW responsible for generation of the secondary wave. Rather, we believe that some other GWs generated by the cloud convections in the afternoon, several hours prior to the occurrence of the MSTID, might be responsible for generation of the secondary GWs. Nevertheless, it is important to note that both the observed MSTIDs and MLT-GWs at the equatorial and low-latitude regions had their origin to the south (30°S), more than 2,500 km away from the observation sites, where the tropospheric deep convection system was active. Therefore, it is likely that the MLT-GWs were generated by the tropospheric cloud convections and the MSTID was induced by a secondary GW in the lower thermosphere. Vadas and Crowley (2010) have reported a similar case from North America.

5. Conclusion

On 16–17 September 2015, we observed MSTIDs, EPBs, and MLT-GWs in the equatorial and low- to middle-latitude (0–30°S) region during the afternoon to evening hours. It was observed that the EPBs occurred when one of the MSTID crests crossed the solar terminator at the time of evening uplift of the ionosphere. The interbubble distance was likely the horizontal wavelength of the MSTID.

The observed MSTIDs had its origin to the south (29°S, 51°W), propagating in a form of concentric waves, with the horizontal wavelength of 646 km and the phase speed of 455 m/s, propagated up to (5°S, 45°W). From the fast phase speed of propagation in the thermosphere, we concluded that the MSTIDs were induced in the thermosphere by a secondary GW created from the dissipation of primary GWs generated by tropospheric cloud convections to the south. This picture is consistent with that presented by Makela et al. (2010) and Vadas and Crowley (2010).

The observed MLT-GWs were likely generated by the tropospheric cloud convections in the same region where the primary GWs occurred that created the secondary GWs which induced the MSTIDs. These observational evidences support that deep cloud convections 2,500 km south of the equator could be responsible for generation of the EPBs.

Data Availability Statement

GNSS ground-based receiver data (RINEX format), airglow image data, and ionosonde data used in the present study are available at EMBRACE data center website (<http://www2.inpe.br/climaespacial/portal/en/#>). The satellite infrared thermal images (Figure 11) are obtained from the Geostationary Operational Environmental Satellite System 13 (GOES 13) data (<http://satellite.cptec.inpe.br/home/index.jsp>). This is due to scientific cooperation between the GOES 13 and the Center for Weather Forecasting and Climate Studies (CPTEC) in Brazil. Two atmospheric models were used in computing the GW ray tracing (Figure 11 and 12): one is Thermosphere–Ionosphere–Electrodynamics General Circulation Model (TIE-GCM) (Roble & Ridley, 1994), which is accessible at TIE-GCM web page (<http://www.hao.ucar.edu/modeling/tgcm>), and the other is the empirical Horizontal Wind Model (HWM07) (Drob et al., 2008).

References

- Abdu, M. A. (2005). Equatorial ionosphere–thermosphere system: Electrodynamics and irregularities. *Advances in Space Research*, 35(5), 771–787. <https://doi.org/10.1016/j.asr.2005.03.150>
- Abdu, M. A., Bittencourt, J. A., & Batista, I. S. (1981). Magnetic declination control of the equatorial F region dynamo electric field development and spread F. *Journal of Geophysical Research*, 86(A13), 11,443–11,446. <https://doi.org/10.1029/JA086iA13p11443>
- Abdu, M. A., Kherani, E. A., Batista, I. S., de Paula, E. R., Fritts, D. C., & Sobral, J. H. A. (2009). Gravity wave initiation of equatorial spread F/plasma bubble irregularities based on observational data from the SpreadFEx campaign. *Ann. Geophys. Series A, Upper atmosphere and space sciences*, 27, 2607–2622.
- Azeem, I., Yue, J., Hoffmann, L., Miller, S. D., Straka, W. C. III, & Crowley, G. (2015). Multisensor profiling of a concentric gravity wave event propagating from the troposphere to the ionosphere. *Geophysical Research Letters*, 42, 7874–7880. <https://doi.org/10.1002/2015GL065903>

Acknowledgments

The present work was supported by CNPq (Conselho Nacional de Pesquisa e desenvolvimento) under the grants 305461/2015-0, 150569/2017-3, 161894/2015-1, and 303511/2017-6; Fundação de Amparo à Pesquisa do Estado de São Paulo (FAPESP) under the grant 2018/09066-8; and Coordenação de Aperfeiçoamento de Pessoal de Nível Superior (CAPES) under the process BEX4488/14-8. K. Shiokawa and Y. Otsuka also thank the Japan Society for Promotion of Science (JSPS) KAKENHI (grant JP 15H05815) for support. I. Paulino would like to thank the Fundação de Amparo à Pesquisa do Estado da Paraíba for the PRONEX grant. Our special thanks are given to all of the reviewers who made critical and constructive comments. Improvement of the discussion is mainly owing to their suggestions.

- Barros, D., Takahashi, H., Wrasse, C. M., & Figueiredo, C. A. O. B. (2018). Characteristics of equatorial plasma bubbles observed by TECMap based on ground-based GNSS receivers over South America. *Annales de Geophysique*, *36*(1), 91–100. <https://doi.org/10.5194/angeo-36-91-2018>
- Booker, H. G., & Wells, H. W. (1938). Scattering of radio waves by the F-region of the ionosphere. *Journal of Geophysical Research*, *43*(3), 249. <https://doi.org/10.1029/TE043i003p00249>
- Drob, D. P., Emmert, J. T., Crowley, G., Picone, J. M., Shepherd, G. G., Skinner, W., et al. (2008). An empirical model of the Earth's horizontal wind fields: HWM07. *Journal of Geophysical Research*, *113*, A12304. <https://doi.org/10.1029/2008JA013668>
- Figueiredo, C. A. O. B., Takahashi, H., Wrasse, C. M., Otsuka, Y., Shiokawa, K., & Barros, D. (2018). Medium scale traveling ionospheric disturbances observed by detrended total electron content maps over Brazil. *Journal of Geophysical Research: Space Physics*, *123*, 2215–2227. <https://doi.org/10.1002/2017JA025021>
- Fritts, D. C., Vadas, S. L., Riggin, D. M., Abdu, M. A., Batista, I. S., Takahashi, H., et al. (2008). Gravity wave and tidal influences on equatorial spread F based on observations during the spread F experiment (SpreadFEx). *Annales de Geophysique*, *26*(11), 3235–3252. <https://doi.org/10.5194/angeo-26-3235-2008>
- Hocke, K., & Schlegel, K. (1996). A review of atmospheric gravity waves and travelling ionospheric disturbances: 1982–1995. *Annales de Geophysique*, *14*, 917–940.
- Huang, C.-S. (2018). Effects of the postsunset vertical plasma drift on the generation of equatorial spread F. *Progress in Earth and Planetary Science*, *5*(1), 3. <https://doi.org/10.1186/s40645-017-0155-4>
- Huang, C.-S., & Hairston, M. R. (2015). The postsunset vertical plasma drift and its effects on the generation of equatorial plasma bubbles observed by the C/NOFS satellite. *Journal of Geophysical Research: Space Physics*, *120*, 2263–2275. <https://doi.org/10.1002/2014JA020735>
- Huang, C.-S., La BeaujardièRe, O., Roddy, P. A., Hunton, D. E., Ballenthin, J. O., Hairston, M. R., & Pfaff, R. F. (2013). Large-scale quasi-periodic plasma bubbles: C/NOFS observations and causal mechanism. *Journal of Geophysical Research: Space Physics*, *118*, 3602–3612. <https://doi.org/10.1002/jgra.50338>
- Huba, J. D., & Joyce, G. (2010). Global modeling of equatorial plasma bubbles. *Geophysical Research Letters*, *37*, L17104. <https://doi.org/10.1029/2010GL044281>
- Kelley, M. C. (2009). *The Earth's ionosphere: Plasma physics and electrodynamics*, International Geophysics Series 96 (Ch. 4, pp. 142–149). San Diego, USA: Academic Press.
- Makela, J. J., Vadas, S. L., Muryanto, R., Duly, T., & Crowley, G. (2010). Periodic spacing between consecutive equatorial plasma bubbles. *Geophysical Research Letters*, *37*, L14103. <https://doi.org/10.1029/2010GL043968>
- McClure, J. P., Hanson, W. B., & Hoffman, J. H. (1977). Plasma bubbles and irregularities in the equatorial ionosphere. *Journal of Geophysical Research*, *82*(19), 2650–2656. <https://doi.org/10.1029/JA082i019p02650>
- Nicolls, M. J., Vadas, S. L., Aponte, N., & Sulzer, M. P. (2014). Horizontal parameters of daytime thermospheric gravity waves and E region neutral winds over Puerto Rico. *Journal of Geophysical Research: Space Physics*, *119*, 575–600. <https://doi.org/10.1002/2013JA018988>
- Nishioka, M., Tsugawa, T., Kubota, M., & Ishii, M. (2013). Concentric waves and short-period oscillations observed in the ionosphere after the 2013 Moore EF5 tornado. *Geophysical Research Letters*, *40*, 5581–5586. <https://doi.org/10.1002/2013GL057963>
- Otsuka, Y. (2018). Review of the generation mechanisms of post-midnight irregularities in the equatorial and low-latitude ionosphere. *Progress in Earth and Planetary Science*, *5*(1), 57. <https://doi.org/10.1186/s40645-018-0212-7>
- Otsuka, Y., Suzuki, K., Nakagawa, S., Nishioka, M., Shiokawa, K., & Tsugawa, T. (2013). GPS observations of medium-scale traveling ionospheric disturbances over Europe. *Annales de Geophysique*, *31*(2), 163–172. <https://doi.org/10.5194/angeo-31-163-2013>
- Paulino, I., Takahashi, H., Vadas, S. L., Wrasse, C. M., Sobral, J. H. A., Medeiros, A. F., et al. (2012). Forward ray-tracing for medium-scale gravity waves observed during the COPEX campaign. *Journal of Atmospheric and Solar-Terrestrial Physics*, *90-91*(2012), 117–123. <https://doi.org/10.1016/j.jastp.2012.08.006>
- Roble, R. G., & Ridley, E. C. (1994). A thermosphere–ionosphere–mesosphere electrodynamics general circulation model (time-GCM): Equinox solar cycle minimum simulations (30–500 km). *Geophysical Research Letters*, *21*(417–420), 94–8276.
- Sahai, Y., Bittencourt, J. A., Teixeira, N. R., & Takahashi, H. (1981). Plasma irregularities in the tropical F-region detected by OI 7774 Å and 6300 Å nightglow measurements. *Journal of Geophysical Research*, *86*(A5), 3496–3500. <https://doi.org/10.1029/JA086iA05p03496>
- Sobral, J. H. A., Abdu, M. A., Takahashi, H., Taylor, M. J., de Paula, E. R., Zamlutti, C. J., et al. (2002). Ionospheric plasma bubble climatology over Brazil based on 22 years (1977–1998) of 630 nm airglow observations. *Journal of Atmospheric and Solar-Terrestrial Physics*, *64*(12–14), 1517–1524. [https://doi.org/10.1016/S1364-6826\(02\)00089-5](https://doi.org/10.1016/S1364-6826(02)00089-5)
- Takahashi, H., Taylor, M. J., Pautet, P.-D., Medeiros, A. F., Gobbi, D., Wrasse, C. M., et al. (2009). Simultaneous observation of ionospheric plasma bubbles and mesospheric gravity waves during the SpreadFEx Campaign. *Annales Geophysicae*, *27*, 1477–1487. <https://doi.org/10.5194/angeo-27-1477-2009>
- Takahashi, H., Wrasse, C. M., Denardini, C. M., Pádua, M. B., de Paula, E. R., Costa, S. M. A., et al. (2016). Ionospheric TEC weather map over South America. *Space Weather*, *14*, 937–949. <https://doi.org/10.1002/2016SW001474>
- Takahashi, H., Wrasse, C. M., Figueiredo, C. A. O. B., Barros, D., Abdu, M. A., Otsuka, Y., & Shiokawa, K. (2018). Equatorial plasma bubble seeding by MSTIDs in the ionosphere. *Progress in Earth and Planetary Science*, *5*(1), 32. <https://doi.org/10.1186/s40645-018-0189-2>
- Takahashi, H., Wrasse, C. M., Otsuka, Y., Ivo, A., Gomes, V., Paulino, I., et al. (2015). Plasma bubble monitoring by TECMap and 630 nm airglow image. *Journal of Atmospheric and Solar-Terrestrial Physics*, *130-131*, 151–158. <https://doi.org/10.1016/j.jastp.2015.06.003>
- Tsuda, T., Nishida, M., Rocken, C., & Ware, R. H. (2000). A global morphology of gravity wave activity in the stratosphere revealed by the GPS occultation data (GPS/MET). *Journal of Geophysical Research*, *105*(D6), 7257–7273. <https://doi.org/10.1029/1999JD901005>
- Tsunoda, R. T. (2015). Upwelling: A unit of disturbance in equatorial spread F. *Progress in Earth and Planetary Science*, *2*(1), 9. <https://doi.org/10.1186/s40645-015-0038-5>
- Tsunoda, R. T., Saito, S., & Nguyen, T. T. (2018). Post-sunset rise of equatorial F layer—Or upwelling growth? *Progress in Earth and Planetary Science*, *5*(1), 22. <https://doi.org/10.1186/s40645-018-0179-4>
- Tsunoda, R. T., Yamamoto, M., Tsugawa, T., Hoang, T. L., Tulasi Ram, S., Thampi, S. V., et al. (2011). On seeding large-scale wave structure equatorial spread F and scintillations over Vietnam. *Geophysical Research Letters*, *38*, L20102. <https://doi.org/10.1029/2011GL049173>
- Tulasi Ram, S., Yamamoto, M., Tsunoda, R. T., Chau, H. D., Hoang, T. L., Damtie, B., et al. (2014). Characteristics of large-scale wave structure observed from African and Southeast Asian longitudinal sectors. *Journal of Geophysical Research: Space Physics*, *119*, 2288–2297. <https://doi.org/10.1002/2013JA019712>
- Vadas, S. L., & Crowley, G. (2010). Sources of the traveling ionospheric disturbances observed by the ionospheric TIDDBIT sounder near Wallops Island on 30 October 2007. *Journal of Geophysical Research*, *115*, A07324. <https://doi.org/10.1029/2009JA015053>

- Vadas, S. L., & Fritts, D. C. (2002). The importance of spatial variability in the generation of secondary gravity waves from local body forces. *Geophysical Research Letters*, *29*(20), 45-1–45-4. <https://doi.org/10.1029/2002GL015574>
- Vadas, S. L., & Liu, H. (2009). Generation of large-scale gravity waves and neutral winds in the thermosphere from the dissipation of convectively generated gravity waves. *Journal of Geophysical Research*, *114*, A10310. <https://doi.org/10.1029/2009JA014108>
- Vadas, S. L., & Liu, H.-L. (2013). Numerical modeling of the large-scale neutral and plasma responses to the bodyforces created by the dissipation of gravity waves from 6 h of deep convection in Brazil. *Journal of Geophysical Research: Space Physics*, *118*, 2593–2617. <https://doi.org/10.1002/jgra.50249>
- Vadas, S. L., Taylor, M. J., Pautet, P.-D., Stamus, P. A., Fritts, D. C., Liu, H.-L., et al. (2009). Convection: The likely source of the medium-scale gravity waves observed in the OH airglow layer near Brasília, Brazil, during the SpreadFEX campaign. *Annales de Geophysique*, *27*(1), 231–259. <http://www.ann-geophys.net/27/231/2009/>, <https://doi.org/10.5194/angeo-27-231-2009>
- Vadas, S. L., Xu, S., Yue, J., Bossert, K., Becker, E., & Baumgarten, G. (2019). Characteristics of the quiet-time hot spot gravity waves observed by GOCE over the Southern Andes on 5 July 2010. *Journal of Geophysical Research: Space Physics*, *124*(8), 7034–7061. <https://doi.org/10.1029/2019JA026693>
- Vadas, S. L., Yue, J., She, C.-Y., Stamus, P. A., & Liu, A. Z. (2009). A model study of the effects of winds on concentric rings of gravity waves from a convective plume near Fort Collins on 11 May 2004. *Journal of Geophysical Research*, *114*, D06103. <https://doi.org/10.1029/2008JD010753>
- Weber, E. J., Buchau, J., Eather, R. H., & Mende, S. B. (1978). North–south aligned equatorial airglow depletions. *Journal of Geophysical Research*, *83*(A2), 712–716. <https://doi.org/10.1029/JA083iA02p00712>
- Yokoyama, T. (2017). A review on the numerical simulation of equatorial plasma bubbles toward scintillation evaluation and forecasting. *Progress in Earth and Planetary Science*, *4*(1), 37. <https://doi.org/10.1186/s40645-017-0153-6>